Unsteady characteristics of pressure and swirl distortion in helicopter intake: A lattice Boltzmann method approach

Alexandre Di-Marco, Jerome Jacob, Pierre Sagaut

To cite this version:

Alexandre Di-Marco, Jerome Jacob, Pierre Sagaut. Unsteady characteristics of pressure and swirl distortion in helicopter intake: A lattice Boltzmann method approach. Aerospace Science and Technology, 2023, 138, pp.108333. 10.1016/j.ast.2023.108333 . hal-04543807

HAL Id: hal-04543807
https://hal.science/hal-04543807v1

Unsteady characteristics of pressure and swirl distortion in helicopter intake: A lattice Boltzmann method approach

Alexandre Di-Marco [*], Jerome Jacob, Pierre Sagaut

Aix Marseille Univ, CNRS, Centrale Marseille, M2P2 UMR 7340, Marseille, France

ARTICLE INFO

Article history:
Received 29 November 2022
Received in revised form 31 March 2023
Accepted 11 April 2023
Available online 17 April 2023
Communicated by Damiano Casalino

Keywords:
Lattice Boltzmann method
Pressure distortion
Swirl distortion
Air intake unsteady flow distortion

ABSTRACT

The present paper focuses on the analysis of the unsteady characteristics of pressure and swirl distortion and their relationship inside a complex air intake, including a plenum chamber, using Large-Eddy Simulation based on the lattice Boltzmann method (LBM). The steady-state analysis of the pressure field and swirl angle in the Aerodynamic Interface Plane (AIP) shows a complex pressure and swirl distortion pattern, as well as a high level of unsteadiness. Additionally, two vortical structures with equal intensity located on the top and bottom sides of the AIP plane were identified. The unsteady pressure distortion analysis highlighted fluctuations between two positions of the maximum circumferential pressure distortion in the AIP plane. One of these positions presents mean and peak distortion values lower than the other position. Furthermore, an alternating vortex pattern between two swirl patterns in the AIP plane is also identified. Finally, the relationship between pressure and swirl unsteadiness was investigated, and a link between the swirl distortion pattern and pressure distortion was identified. The identification of this relationship will allow geometrical changes in the air intake, leading to a reduction of the average circumferential distortion level, as well as a reduction of the maximum peak level achievable during a flight phase.

1. Introduction

Within the last few years, aircraft engines have been increasingly integrated inside the aircraft. However, this high degree of integration makes air intake geometry more and more complex, leading to a more complex distortion pattern of the flow field entering the engine. It exist several type of distortion [1], including total pressure, temperature and swirl distortion. Numerous studies have shown that steady distortion leads to a strong reduction in surge margin [2–5], as well as a significant impact on engine performance [6]. Usually, engine/intake compatibility is assessed during dedicated flight tests or scaling tests where steady-state distortions are measured to verify compliance with the engine. Moreover, these tests are expensive and the instrumentation used does not always allow for the measurement of swirl in flight. Therefore, the risks of a design change at the end of development are significant. Most of the time, distortion of the different physical parameters are studied separately [7–10]. However, some recent studies show that the distortions must be considered together. For example, total pressure and total temperature distortion seem to interact with each other in a linear way, meaning that it is possible to sum up their effects on the surge margin loss to estimate the impact of the coupled effects on surge margin [4]. The effects of the combination of planar wave and total pressure distortion are unknown and the SAE [11] recommends verifying the impact on surge margin while these effects are combined. On the other hand, some studies highlight that total pressure distortion and swirl together interact in a nonlinear way [12,13]. Indeed, the SAE [5] shows that a co-swirl coupled with total pressure distortion has a greater impact on surge margin. On the other hand, counter-swirl coupled with pressure distortion has less impact on surge margin. In addition, different types of swirls have shown various impacts on surge margin. Fredrick et al. [14] compared the effect of different types of swirls on surge margin and showed that twin swirl has less impact on surge margin than bulk swirl. Therefore, total pressure distortion and swirl are key parameters for air intake/aircraft compatibility. Early estimation of total pressure distortion and swirl is a major issue for the aircraft manufacturer to reduce risk and costs.

Engine/aircraft compatibility does not only rely on steady state value of pressure distortion and swirl. Recent developments have shown the importance of taking dynamic distortion into account. Unsteady distortion can impact engine stability and performance [15], leading to stall inception mechanisms in aero-engine com-

---

[*] Corresponding author.
E-mail address: Alexandre.di-marco@airbus.com (A. Di-Marco).

Nomenclature

AIP	] Aerodynamic Interface Plane	SAE	Society of Automotive Engineers
APU	Auxiliary Power Unit	$\frac{\Delta PC}{P}$	Circumferential pressure distortion descriptor
CDI	Circumferential Distortion Index	$\frac{\Delta PR}{P}$	Radial pressure distortion descriptor
CFD	Computational Fluid Dynamics	DC_{60}	Total pressure distortion descriptors on 60°
LBM	Lattice Boltzmann Method	α	Swirl Angle
PDF	Probability Density Function	SI	Swirl Intensity descriptor
PIV	Particle image velocimetry	SP	Swirl Pairs descriptors
PSD	Power Spectral Density	SD	Swirl Directivity descriptors
RDI	Radial Distortion Index	θ	Extent

pressors [16], and can be triggered by localized peak fluctuations of pressure, vorticity, and velocity [17]. Unsteady distortions can occur in normal flight conditions and can be generated by both internal and external causes.

However, the unsteadiness of the flow field in AIP plane is difficult to study, the elaboration of a representative test is complicated, and capturing unsteady phenomena requires expensive specific instrumentation such as the use of specific five hole pressure rake placed in AIP plane as prescribed in the SAE ARP1420C technical report [6] or the use of non intrusive measurement like PIV [18] or some new non intrusive method highlight in Doll et al. [19]. The first studies on dynamic distortion go back to the 1970's with Jacocks [20] who is one of the first to be interested in the dynamic aspect of distortion and in particular the determination of the maximum time variant distortion level. Several other studies were conducted to determine the maximum time variant distortion level depending on the degree of knowledge of the unsteadiness of the flow field entering in the engine. Auleha and Schmitz [21] proposed a basic way with little knowledge about the unsteadiness of the flow. Borg [22] and also Liang and Zhang [23] proposed two similar methods, a little more developed based on probability density function and finally Jacocks [20] who uses the extreme value theory to determine the maximum time variant distortion level that can be reached during a flight phase. More recently, Tanguy et al. [24] and Lakebrink and Mani [25] measured unsteady distortion using rakes of high frequency response transducers.

However, despite the conducted studies, no consensus has been reached on the best way to determine the maximum time variant distortion level. Moreover all these studies share the fact of being based on tests, which might be complex and highly expensive to perform in an industrial development context.

Within the last few decades, the improvement of computational capacity and computational fluid dynamics (CFD) now makes it possible to simulate the flow in this type of air intake and also its dynamic behavior. These progresses have allowed to boost the studies about dynamic distortion by using CFD in order to obtain additional information on the flow field which is not available during the tests. Numerous studies are about the assessment of the flow distortion associated with different S-duct or L-duct [26] configurations. Experimental study conducted by Wellborn et al. [27] highlight the presence of a paired swirl in the AIP plane. Other experimental studies performed using SPIV show the necessity to account for the unsteadiness of the flow field such as Gil-Prieto et al. [28] who identify a switching mode between the two swirls. Moreover, Migliorini et al. [29,30] study the impact of non-uniform inlet flow condition on S-duct and highlight that inlet vortices and pressure profiles affect swirl angle unsteadiness and peak swirl intensity as well as extreme value theory predict peak distortion. Experimental studies have shown the complexity of the flow field inside S-duct and the necessity to consider its unsteadiness. Based on these experimental studies, several steady state simulation have been performed using various turbulence models such as the Wray-Agarwal one-equation turbulence model [31] and four different turbulence models in the work of Fiola and Agarwal [32,33]. Additionally, the work of Aref et al. [34] and Delot and Scharnhorst [35] have focused on the validation of different turbulence models and compared their results with the experimental data of Wellborn et al. [27], showing that steady state simulation can be performed with several turbulence models that are able to capture the flow physics. Zhang and Vahdati [36] conducted a parametric study to investigate the effects of inlet distortion on fan aerodynamic stability. They analyzed the distortion by imposing different inlet profiles and concluded that the distortion level had a significant impact on the aerodynamic stability of the fan, while Piovesan et al. [37] investigated the unsteady aerodynamic characteristics for intakes at crosswind. Moreover, Lima et al. [38] conducted numerical investigations of S-shaped air inlets for embedded engines. They studied the effect of the inlet angle on the aerodynamic performance and concluded that the inlet angle had a significant impact on the pressure recovery and the flow distortion in the inlet. Batista de Jesus et al. [39] studied the grid topology of the S-duct inlet with vortex generators, and concluded that the use of vortex generators was an effective way to reduce the distortion level in the S-duct. Additionally, Garbo and German [40] compared adaptive design space exploration methods applied to S-duct CFD simulation. Wojewodka et al. [41] reviewed flow control techniques and optimization in S-shaped ducts and conducted a numerical study of complex flow physics and coherent structures of the flow through a convoluted duct. For the assessment of the unsteadiness of the flow field in a S-duct, several numerical studies were conducted [42,43], MacManus et al. [44] simulated the same test case conduct by Wellborn et al. [27] using Delayed Detached-Eddy Simulation (DDES) and show the ability of this method to simulate well the unsteady behavior of the flow field. Gil-Prieto et al. [45] proposed a method to assess the unsteady flow distortion with numerical simulation and use joint-PDF to identify switching mode and use Extreme Value Theory to determine the time variant distortion level. All these studies have shown the ability of CFD to simulate the steady state and unsteady behavior of the flow field, however for the unsteady behavior, the computational time for these methods is too long to be used in an industrial context.

In the early 2000's, a new highly parallelizable CFD methods called lattice Boltzmann method (LBM) is gaining traction in the academic [46] and industrial [47,48] field. This CFD method differs from the others which are based on macroscopic approach and solve the Navier-Stokes equation. The LBM is based on a mesoscopic approach to solve the fluid dynamic equations. This method is derived from gas kinetics theory with Boltzmann equation and consists in considering a characteristic population of particles to represent the behavior of a fluid at the macroscopic level. Moreover, the LBM method is intrinsically unsteady and the calculation time is extremely reduced compared to the classic calculation code. LBM has already been used for unsteady swirl distortion characteristics assessment and shows its ability to predict the unsteady flow field [49]. However, this study highlights a discrepancy between the magnitude of the predicted and measured unsteadiness properties. Nonetheless, the use of a minimum mesh requirement and a fast convergence solver allows for the investigation of dynamic distortion in an industrial context.

A key focus of this paper is the use of computational fluid dynamics (CFD), more precisely Large-Eddy Simulation in the present work) based on lattice Boltzmann method (LBM) to assess the unsteady aerodynamic characteristics of complex air intake with plenum chamber. Indeed, complex air intake with a plenum chamber is widely used in aeronautics, especially for APU air intake, or on helicopters because of their environmental robustness. The particularity of this air intake is that the air once entered the plenum chamber turns in the plenum before being aspirated by the engine. Moreover, when the air goes to the engine, it has to pass through struts, which disturb the flow [50]. This particularity has the impact of increasing the complexity of the distortion pattern. These activities take part in a broader project, for which the overall objective is to develop a framework that evaluates the combined engine and aircraft configuration for a specific flight mission and that could be applied at the preliminary design stage. Within this framework, engine/intake compatibility and engine performance have to be evaluated for each configuration. Previous study has shown the ability of LBM to simulate the flow field entering the engine and compare steady state parameters simulated by CFD with helicopter flight test results [51]. Furthermore, a complete steady state analysis of the flow field has been performed [52]. However, the unsteady aerodynamic characteristics of this type of air intake with a plenum chamber have never been studied.

In this context, the main objective of the current paper is to improve knowledge in terms of the unsteady characteristics of total pressure distortion and swirl distortion for a complex air intake with a plenum chamber. In Section 2, the main methodology elements of the present study are presented, including the configuration of interest (Sec. 2.1 and Sec. 2.2), the detail of the numerical method (Sec. 2.3), the definition of the different metrics (Sec. 2.4) and a validation of the method (Sec. 2.6). Section 3 is devoted to the analysis of the results, with first, a description and analysis of the unsteady flow field in the air intake (Sec. 3.1), then an analysis of the time averaged and standard deviation of pressure and swirl angle at the AIP plane (Sec. 3.2). Then, unsteady characteristics of total pressure (Sec. 3.3) and swirl distortion (Sec. 3.4) are investigated separately. Finally, the link between the unsteady characteristics of the total pressure distortion and swirl distortion is studied (Sec. 3.5). Conclusions of the present work are given in Section 4.

2. Methodology

2.1. Geometry description

In this paper, the geometry (see Fig. 1) corresponds to a so-called semi-dynamic helicopter air intake, i.e. it is the result of a trade-off between a static air intake which has an extremely low dynamic pressure recovery coefficient and a dynamic air intake with a higher dynamic pressure recovery coefficient. The air intake is composed of a first straight section which comes out of the fuselage of the helicopter and which will ingest the boundary layer generated by the fuselage as shown on Figs. 1a and 1c. At the end of this section is positioned an elbow which will direct the air toward a plenum. The air will then turn in the plenum and be sucked in by the engine. In order to reduce the pressure distortion generated by the plenum, a plenum schim is added. Finally, when the air goes to the engine, it passes through struts that disrupt the flow field. For reasons of confidentiality, the precise characteristics of the air intake cannot be provided.

Table 1
Radial position of each ring of rake.

Ring	R_{ring}/R_{max}
1	0.45
2	0.58
3	0.7
4	0.83
5	0.95

2.2. Case study

The case study presented in this paper is representative of an helicopter in level flight at 140kts with an engine operating condition of about 900kW. To be representative of this case study, the computation domain (Fig. 1b) includes a complete helicopter without tail boom and rotor, with an air intake corresponding to the geometry in Fig. 1 located on the right side of the helicopter. The helicopter geometry is inserted in a parallelepipedic domain where a constant velocity corresponding to the realistic flight condition is imposed at the inlet. The atmospheric pressure is then imposed on the domain's lateral boundaries and outlet. Turbulent wall model [53] is applied on the helicopter and air intake walls in order to model the turbulent boundary layers. To simulate the flow entering the engine, a mass flow rate condition corresponding to the realistic flight conditions is applied at the compressor inlet located at 10 AIP diameter from the AIP plane (see Fig. 1a) so that the flow condition does not influence the results obtained at the AIP plane. The rotor flow is not simulated in the present paper since only level flight is studied. Indeed, during level flight, the rotor is inclined towards the front of the helicopter, while the rotor flow is directed towards the back of the helicopter. Moreover the speed of the helicopter allows to neglect the impact of the rotor flow in this simulation. To assess pressure and swirl distortion, several sensors are placed in the simulation in the AIP plane. Fig. 1a shows the distribution of the sensors in the AIP plane. The Society of Automotive Engineers (SAE) [2] proposes to use 40 probes to catch a typical pressure pattern (8 rakes of 5 probes). However, for more complex inlets they also propose to divide into circumferential sections with greater detail Therefore the sensors pattern used for this study is the following are equally distributed, radially and circumferentially with 5 radial positions and 18 circumferential positions. Table 1 shows the radial position of each ring. For the validation study, additional numerical sensor are placed in the simulation at the same place as the sensor used during flight test. Due to space constraints and the risk of surge during flight testing, fewer sensors are used, with only 9 circumferential positions and 4 radial position.

In order to obtain a complete unsteady solution, a simulation time of approximately 100 convective times estimated from the average axial velocity at the reference plane and the length of the air intake mean line is considered. However, only the final 60 convective times were analyzed during post-processing to exclude the initial transient phase from the steady state to the fully established unsteady solution.

2.3. LBM

CFD simulations presented in the present manuscript were performed with the ProLB software, which uses the lattice Boltzmann method [54]. This method is based on the resolution of the Boltz-

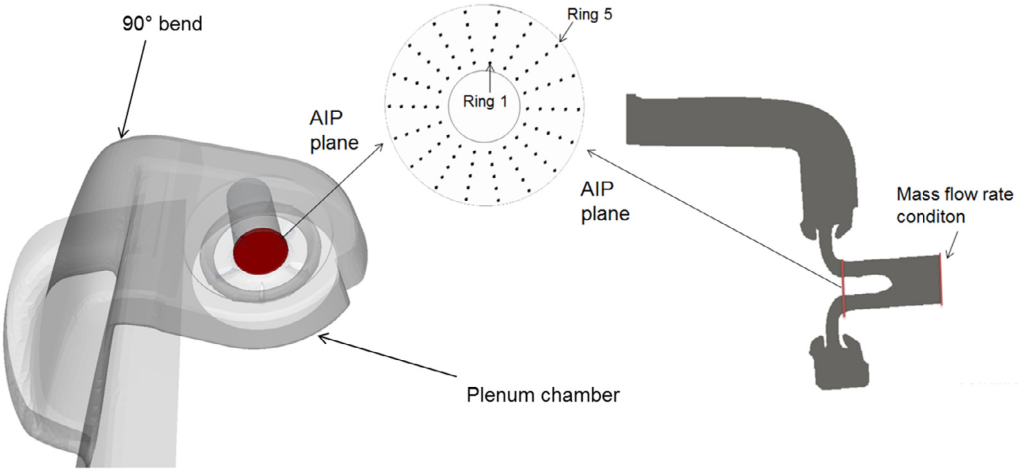

(a) Visualization of the AIP plane and probes locations in the air intake

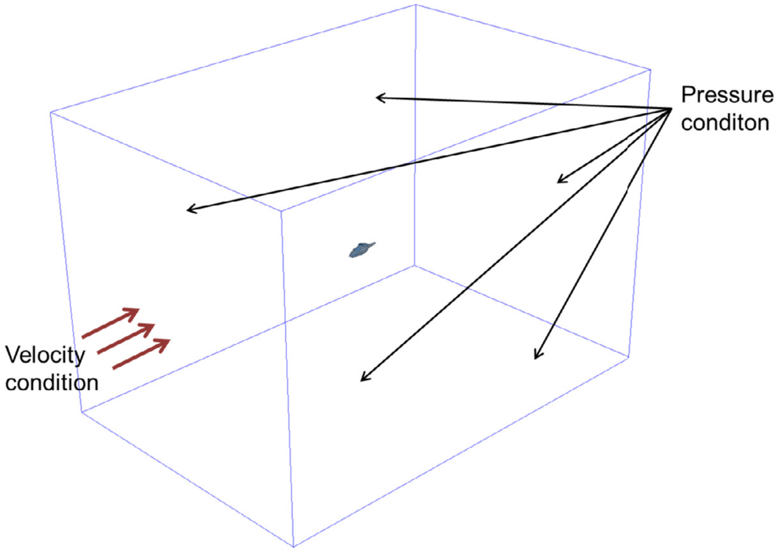

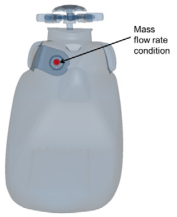

(c) Front view of the helicopter geometry with location of the air intake and AIP plane

(b) Computational domain and boundary conditions

Fig. 1. Visualization of the air intake geometry and numerical configuration.

mann equation (Eq. (1)) describing the evolution of a particle distribution function $f = f(\vec{x}, \vec{c}, t)$ which is related to the probability density of particles with velocity $\vec{c}$ at position $\vec{x}$ and time t.

$$\frac{df}{dt} + \vec{c} \cdot \vec{\nabla} f = \Omega(f) \tag{1}$$

The Boltzmann equation is then discretized in the velocity space on a D3Q19 lattice in the present manuscript, corresponding to a 3 dimensional lattice with 19 discrete velocities, leading to the lattice Boltzmann equation (Eq. (2))

$$f_\alpha(\vec{x} + \vec{c_\alpha} dt, t + dt) - f_\alpha(\vec{x}, t) = \Omega_\alpha(\vec{x}, t) \tag{2}$$

where f_α represents the distribution function in the α direction of the lattice and Ω_α is the collision operator associated with it. In general, equation (2) is solved in two steps using a Strang-type splitting, first, the post collision function $f_\alpha^{coll}(\vec{x}, t) = f_\alpha(\vec{x}, t) + \Omega_\alpha(\vec{x}, t)$ is computed, then it is propagated to the neighboring points. The usual macroscopic quantities (density ρ and velocity components u_i) can then be computed from the moments of distribution function as follows.

$$\rho = \sum_{\alpha=0}^{18} f_\alpha \tag{3a}$$

$$\rho\, u_i = \sum_{\alpha=0}^{18} f_\alpha\, c_{\alpha,i} \tag{3b}$$

In the present manuscript, the collision operator used is the Hybrid Recursive Regularized (HRR) model presented in Jacob et al. [55] and the Shear Improved Smagorinsky Model [56] (SISM) is used to model subgrid scales.

In practice, the lattice Boltzmann equation is solved on non body fitted grids based on a hierarchy of embedded cartesian grids with a ratio of 2 between the grid spacing of two successive refinement levels (see Refs. [55,57,46] for grid examples). This strategy allows for an easy meshing of complex geometry, such as the complete helicopter equipped with a realistic air intake geometry, including a plenum chamber study in the present manuscript.

2.4. Total pressure and swirl distortion metrics

The present study is focused on total pressure and swirl distortion. To quantify and characterize the distortion, several param-

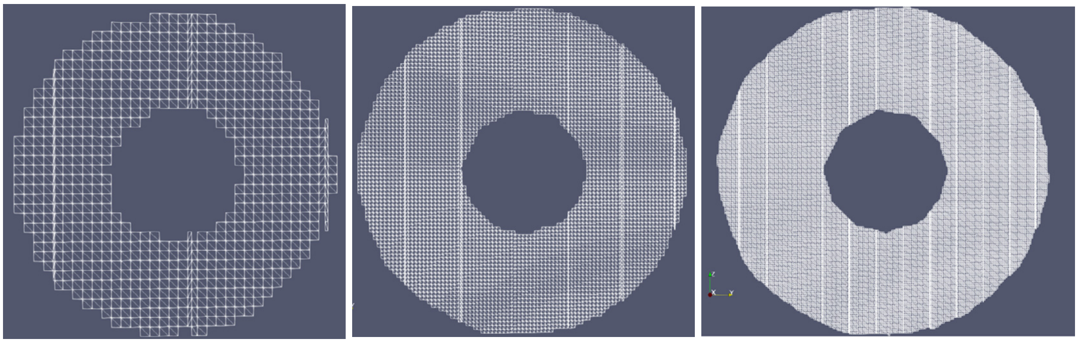
(a) Coarse grid level (b) Medium grid level (c) Fine grid level

Fig. 2. Visualization of the grid in the AIP plane for the 3 mesh resolution used in the sensitivity analysis.

eters have been defined in the literature. For example, KD and KA index developed by Pratt & Whitney [58], $K\theta$ and Kr parameters developed by Naval Air Propulsion Center [59], Rolls Royce θ critical indices (DC_θ) describe in ref [60], GE Method D system describe in ref [61] CDI and RDI proposed by the SAE [2]. All these parameters were created to be able to experimentally quantify the decrease in the surge margin related to total pressure distortion. The same parameters are created to characterize swirl distortion.

However, in the present study, the following parameters introduced in the SAE technical reports [2,5] are used for pressure and swirl distortion characterization.

1. Pressure distortion
   - Circumferential total distortion ($\frac{\Delta PC}{P}$) allows to describe the non uniformity of the pressure field on a ring and to quantify the amplitude of the total pressure distortion weighted by the size of the low pressure area. Indeed, taking into account the size of the distortion is important because it allows to have an indication on the time that the compressor blade will spend in the low pressure area during a revolution period and has a direct impact on engine stability [7]. The amplitude allows to give an information on the variation of the aerodynamic load that the blade will subjected in the low pressure area.
   - Radial total pressure distortion ($\frac{\Delta PR}{P}$) allows to describe the radial non uniformity of the pressure field and to quantify The radial distortion has for impact a radial variation of the aerodynamic load of the blade. It was shown that this distortion has a greater impact than the circumferential pressure distortion on the stability of the engine [2,62].
2. Swirl distortion
   - Swirl Intensity (SI) is based on the swirl angle distribution on a ring. This parameter represents the averaged absolute swirl angle on a ring intensity of the swirl. For the compressor, this parameter represents a change in the angle of attack of the blade. This will have an impact on the aerodynamic load of the blade.
   - Swirl Pairs (SP) Swirl Pairs indicate the numbers of pairs swirl in the ring. This parameter is used for identify swirling vortical structures. For example, a $SP = 1$ mean that there is 2 swirling vortical structure which turns in the opposite direction.
   - Swirl Directivity (SD) describe the main direction of the swirl. In this study, a positive value of swirl is define as clockwise direction and a negative value of swirl as a counterclockwise direction.

A more detailed explanation of these parameters and their associated mathematical formulations are presented in appendix A for the total pressure distortion and appendix B for the swirl distortion.

2.5. Grid sensitivity

As seen previously in part 2.3, the grid used in LBM is a Cartesian grid; therefore, an assessment of the grid sensitivity is performed. In this paper, 3 type of grid are evaluated in term of time to perform the simulation and deviation from the fine grid. This grid sensitivity analysis is performed on the mean pressure, DC_{60} and mean swirl in the AIP plane considering a coarse (Fig. 2a), medium (Fig. 2b) and fine grid (Fig. 2c) with respectively 11, 28, and 55 points in the annular radius of the AIP plane.

Fig. 3 shows the grid sensitivity. The x axis corresponds to grid level, and the y-axis corresponds to the deviation from fine grid of DC_{60}, AIP mean pressure, and mean Swirl in the AIP plane. The axis on the right corresponds to the time to perform a simulation. Fig. 3a shows the convergence analysis for mean pressure; a deviation of up to 1% was observed for the average pressure value in the fine mesh. However, this deviation was significantly reduced to 0.05% for the medium and high mesh levels, indicating a low deviation between the calculated average pressure values. Moreover, a substantial increase in computation time was observed between the three mesh levels. The pressure distortion, Fig. 3b, was selected as a key parameter in this study as it was found to have a deviation of almost 70% for the coarse mesh level compared to the fine mesh level. However, for the medium mesh level, a deviation of only 10% was observed, which was considered acceptable for this study. Finally, the swirl in the AIP plane, Fig. 3c was also investigated, and a deviation of over 1° was observed for the coarse mesh level, while only a 0.2° deviation was observed for the medium mesh level, which was acceptable for this study. Based on these findings, it can be concluded that the first mesh level did not converge, and therefore, the second mesh level was chosen, which had a computation time 40% lower than that of the fine mesh level. This was essential for industrial applications where minimizing computation time is crucial.

Based on the obtained results, we have selected the medium grid level as it offers a favorable balance between simulation time and deviation from the fine grid. The resulting mesh size leads to an average Y+ value of approximately 100 throughout the entire air intake. However, it should be noted that this value may vary significantly considering that the distance of the first node to the wall ranges between 0 and $\sqrt{3}dx$, corresponding to the diagonal of the cubic cell.

2.6. CFD validation

CFD simulation is validated by comparing the steady state parameters like pressure drop (ΔP) and pressure distortion (DC_{60})

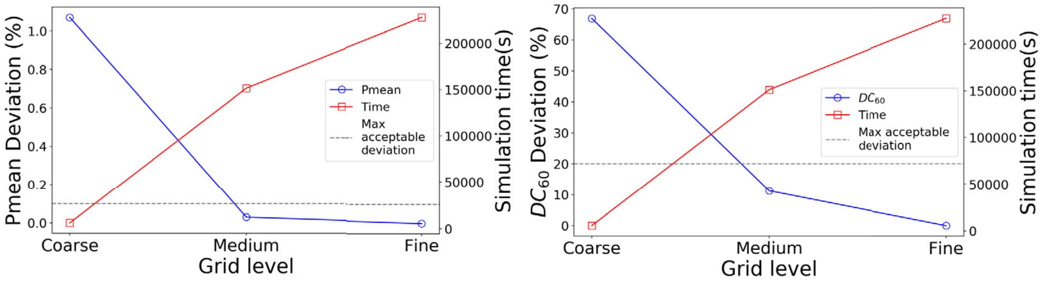

(a) Convergence analysis of Pmean in AIP

(b) Convergence analysis of DC_{60} in AIP

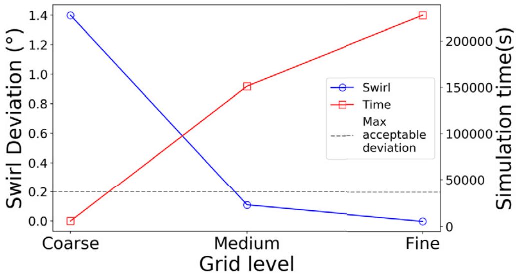

(c) Convergence analysis of mean Swirl in AIP

Fig. 3. Grid sensitivity.

Table 2
Numerical simulation validation test case for different flight test.

Case	P0 (Pa)	OAT (K)	IAS	N1 (%)
1	97 446	297.7	100kts	94.2
2	100 985	296.2	97kts	92.6
3	100 881	296	114kts	94.2
4	96 832	291	140kts	97.7
5	97 241	297.7	140kts	98.5

Table 3
Numerical simulation deviation for DC_{60} and ΔP for each validation test case in Table 2.

Case	ΔP(%)	DC_{60}
1	-0.6	0.02
2	0.3	0.01
3	0.3	0.01
4	-0.02	0.05
5	-0.2	0
Mean Deviation	-0.03	0.02

with those obtained during a dedicated flight test. During these flight tests, the air intake is equipped with 36 pressure sensors located at the AIP. These sensors are located at 9 different circumferential positions and 4 different radial locations in order to ensure that circumferential and radial distortions are accounted for. In the present validation, 5 different configurations summarized in Table 2 are considered with different values for the P0, OAT, IAS, and N1 parameters. The swirl cannot be measured in flight since the position of the AIP plane makes the use of 5-hole or 3-hole probes not possible. For this reason, DC_{60} and ΔP are the only quantities considered in the present validation. A more detailed validation can be found in Di-Marco et al. [51].

The difference between CFD and flight tests is considered acceptable, considering the uncertainty of the measurements in flight, if it's lower than 0.5 for the pressure drop in the air intake and, lower than 0.02 for the pressure distortion.

Table 3 show the deviation between flight test results and CFD simulation. The deviation is defined as the difference between the CFD simulation and the flight tests. The pressure drop in the air intake is well simulated even if we observe either an overestimation of the pressure drop (cases 1, 4, and 5) or an underestimation of the pressure drop (cases 2, and 3), depending on the considered case. Pressure distortion is overestimated in all cases. These results suggest that the measurement uncertainties in flight can impact the distortion level, as various parameters like yaw, roll, or pitch angles can affect pressure and swirl distortion, which cannot be fully controlled. The CFD simulation assumes a level flight condition by default, which may not accurately reflect the real flight condition of the helicopter. It is also observed that in cases 1 and 4, the acceptance criterion is exceeded. However, the deviation remains acceptable taking into account the uncertainty of in-flight measurements and the helicopter's position, which are unknown and can have an effect on pressure drop and pressure distortion. From these results, it is considered that the steady state simulation is validated since, in average, the different predicted parameters are in the range of acceptance.

3. Results and discussion

3.1. Visualization of the flow in the air intake

In this section, we visualize the flow through the air intake using four types of visualization shown in Fig. 4. Fig. 4a displays a cross-section of the air intake colored by the pressure field. At the entrance of the air intake, a zone near the wall has a lower pressure value, corresponding to the boundary layer that the air intake ingests. After passing through the plenum chamber, the flow is sucked by the engine. We observed a pressure drop immediately after the 90° bend connected to the engine. Furthermore, the loss associated with the bend is more significant on the bottom side of the figure. Fig. 4b shows the axial velocity along the air intake. We found that the axial velocity is lower inside the boundary layer than outside it. The flow then turns through the first 90° bend, leading to a decrease in axial velocity. After passing through the plenum chamber and the engine's 90° bend, there is a sub-

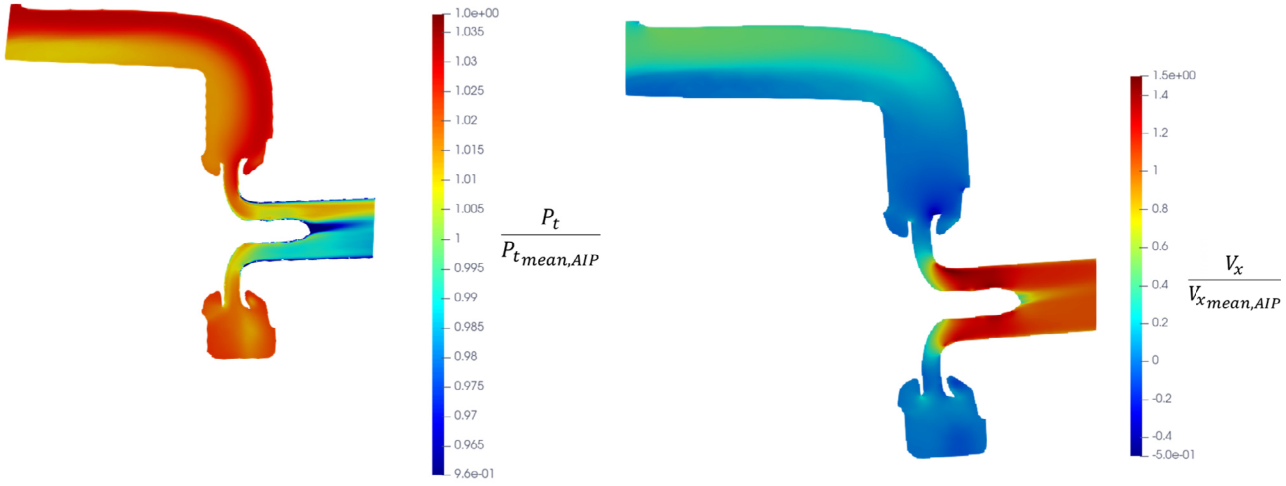

(a) Visualization of pressure field through the air intake

(b) Visualization of axial velocity through the air intake

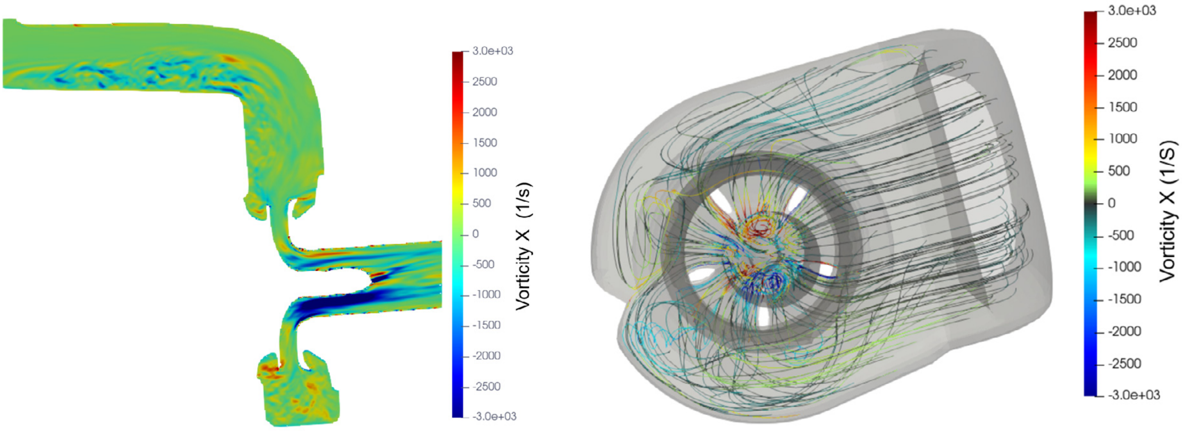

(c) Visualization of vorticity around X axis

(d) vizualisation of streamline in the air intake color by vorticity

Fig. 4. Visualization of the flow field through the air intake. (For interpretation of the colors in the figure(s), the reader is referred to the web version of this article.)

stantial increase in axial velocity. Fig. 4c depicts a cross-section of the vorticity around the X-axis. We observed a slightly negative vorticity zone around the X-axis at the air intake's entrance, corresponding to the boundary layer that developed on the helicopter's fuselage. This boundary layer is then ingested by the air intake. After passing through the 90° bend, the flow enters the plenum. We observed that the vorticity inside the second bend differs between both sides of the plenum, with a considerable zone of negative X vorticity in the bottom duct. Fig. 4d illustrates the streamlines in the air intake, particularly in the plenum. We found that the streamlines that travel the longest distance to the left part of the plenum on the plenum schim side are highly disturbed with high vorticity levels. The streamline directly entering the engine (from the right side) is straight and does not exhibit any rotational effects. On the AIP plane, two vortical structures can be seen, one located on the top side and the other on the bottom side. Further details on these two vortical structures are available in Section 3.2. We observed that the formation of these two vortical structures seems to be induced by the struts, as the streamlines are deviated by their presence when the air is sucked by the engine, leading to significant vorticity effects.

3.2. *Time average and unsteadiness in AIP plane*

In this section, the time average and standard deviation of total pressure and swirl angle at the AIP plane are presented.

Fig. 5a represents the distribution of the total pressure divided by the dynamic pressure at AIP plane and the corresponding standard deviation. Several phenomena can be noticed. First of all, it can be noticed that the left part of the AIP plane is well homogeneous and has a higher pressure level than the rest of the AIP plane. 3 low pressure areas are identified, 1 located on the upper part of the AIP plane and 2 located on its lower part. Moreover, the impact of the struts on the pressure distribution in the AIP plane is noticeable. They generate flow separation [50] that is highlighted by discontinuity in the pressure field visible on the left part in Fig. 5a. The impact of plenum schim can be identified due to high level unsteadiness in the right hand side of the AIP plane. Moreover, a detailed analysis of the steady state parameter in the

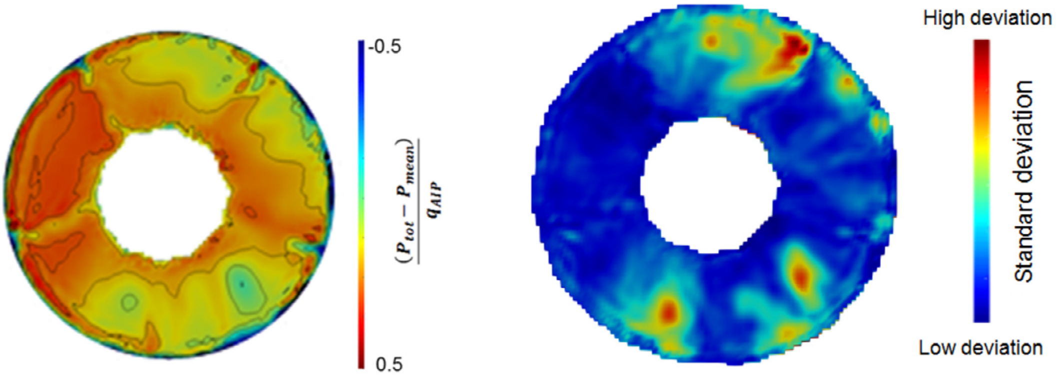

(a) Pressure field in the AIP plane

(b) Non-dimensional standard deviation of pressure in AIP plane

Fig. 5. Pressure field and non-dimensional standard deviation of pressure in AIP plane.

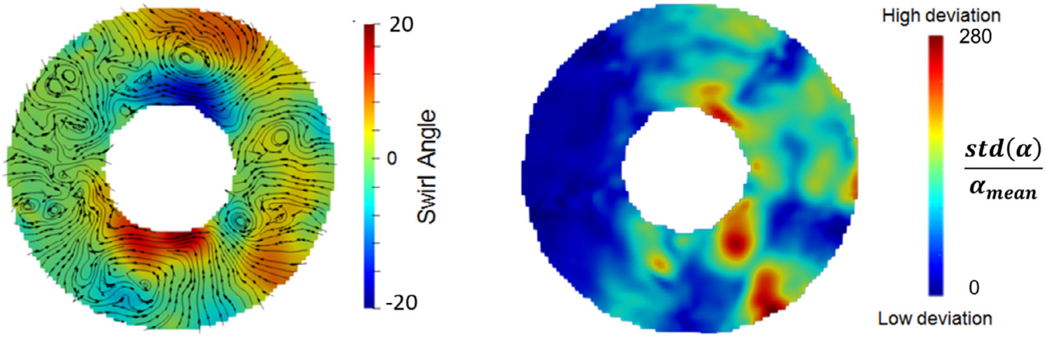

(a) Swirl angle in the AIP plane with streamline

(b) Standard deviation of swirl angle

Fig. 6. Swirl angle pattern and non-dimensional standard deviation of swirl angle in AIP plane.

AIP plane is available in Di-Marco et al. [52]. Fig. 5b shows the standard deviation of the total pressure field. Three areas of high standard deviation located at the same locations as the low pressure areas are identified, which means that the low pressure areas are subject to a strong unsteadiness.

Finally, comparing the pressure field in the AIP plane generated by an air intake with a plenum with an S-duct air intake found in the literature [27,44], it can be noticed that the pressure field pattern is different. Indeed, in the case of a S-duct, the most important pressure drop is located at the bottom of the AIP plane, in our case several pressure drop zone are identified located at the bottom part, top side and left side of the AIP plane.

Fig. 6a shows the distribution of swirl angle in the AIP plane with associated streamline. 2 vortical structure can be noticed, the first one located on the upper part of the AIP plane and the second one in its lower part. The area located on the upper side of the AIP plane has a higher intensity than that the one located on the bottom side. Moreover, the left part of the AIP plane is homogeneous, with a swirl angle of almost zero. On the other hand, the right part is much less homogeneous, with recirculation areas generated by the plenum schim. By looking at Fig. 6b, it can be noticed that the most important standard deviation is located at the right side of the AIP plane. This means that the two vortical structure identified and also the recirculation zone generated by the plenum schim are also subject to a strong unsteadiness as well as a pressure field.

As for the pressure field, we notice that the swirl angle field in the AIP plane is much more different than the one generated by an S-duct air intake. Indeed, on the S-duct, a pairs swirl is identified at the bottom part of the AIP plane. For our air intake, which includes a plenum chamber, two vortical structures are identified, one located at the bottom side and the other on the top side of the AIP plane.

3.3. *Unsteady pressure distortion characteristics*

The results presented in section 3.2 showed a significant unsteadiness of the pressure field in the AIP plane. This part aims to study in more detail the unsteady part of the pressure field in the AIP plane. For this purpose, the circumferential pressure distortion and radial pressure distortion parameters are used to describe the pressure distribution in the AIP plane, and these parameters are studied on each ring (see Fig. 1). In order to study the unsteadiness of the flow field, the position of the maximum circumferential pressure distortion and its associated value are investigated in order to locate the ring where this maximal distortion occurs. For the visualization of the data, joint-PDF is used as proposed by Gil-Prieto et al. [28]. This type of visualization allows us to visualize a couple of parameters and also the number of occurrences of these parameters. A red zone corresponds to a high frequency of occurrence, while a blue zone corresponds to a low frequency of occurrence. For all joint-PDF presented in this paper, joint-PDF is divided in 60 partitions and the resolution of each parameter is described before each figure. With the use of the joint-PDF, it is possible to estimate the probability that a couple of parameters

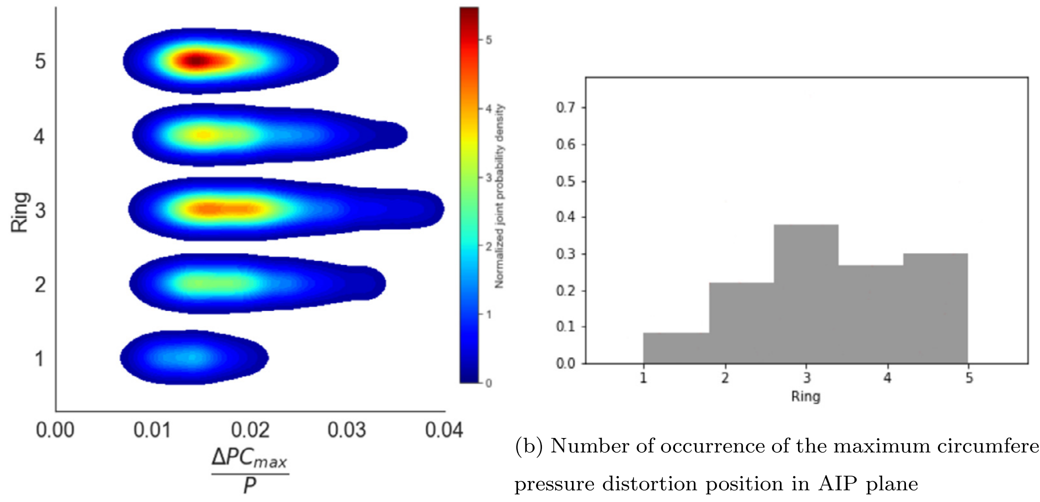

(b) Number of occurrence of the maximum circumferential pressure distortion position in AIP plane

(a) Joint-PDF of value of circumferential pressure distortion and the position on AIP on this distortion

Fig. 7. Joint-PDF of circumferential pressure distortion and its position on AIP, and Histogram of the number of occurrence of where the maximum pressure distortion appear on each ring.

appear. This probability can be calculated with the following formula:

$$P(Y_{low} < Y < Y_{high}, X_{low} < X < X_{high}) = \int_{Y_{low}}^{Y_{high}} \int_{X_{low}}^{X_{high}} PDF \, \mathrm{d}X\mathrm{d}Y \tag{4}$$

Where X corresponds to the parameters on X abscissa in the joint-PDF and Y corresponds to the parameters on Y abscissa. X_{low} and Y_{low} correspond to the lower value of the corresponding parameter, and X_{high} and Y_{high} correspond to the higher value of the corresponding parameter.

Fig. 7a shows the joint-PDF between the radial position of the maximum circumferential pressure distortion and the associated circumferential pressure distortion value. First of all, Fig. 7a shows a higher probability of finding the maximum pressure distortion on the outer rings (3 to 5) than on the inner rings (1 to 2). This figure also highlights a fluctuation between 3 main rings (ring 3,4, and 5). In addition, when the maximum pressure distortion is located on ring 5 it can be noticed that the amplitude of variation is lower than that the one associated with ring 3. However, by looking at the number of occurrences, i.e. the histogram associated with the ring (Fig. 7b), we realize that the position where the maximum pressure distortion is most of the time is on ring 3. From this PDF, the probability of occurrence of the maximum circumferential pressure distortion on this ring is around 30.2% on ring 3, and 21.5% and 24% for rings 4 and 5 respectively. The probability that the maximum circumferential pressure distortion on ring 3 is higher than that on ring 5 can be calculated using equation (4). To do that, the average value of the distortion in ring 5 is calculated. Then the probability that the value of the distortion on ring 3 is higher than the average value of circumferential pressure distortion on ring 5. It can be found that there is 68.2% of probability that the value of circumferential pressure distortion on ring 3 is superior to the value on ring 5, which confirms the first analysis made from the joint-PDF which shows that the pressure distortion associated with ring 3 is much more important than the one associated with ring 5. Moreover, Fig. 7a highlights that the peak distortion associated with a circumferential pressure distortion located on ring 3 is higher than the one reached on ring 5, about 3.5 times higher.

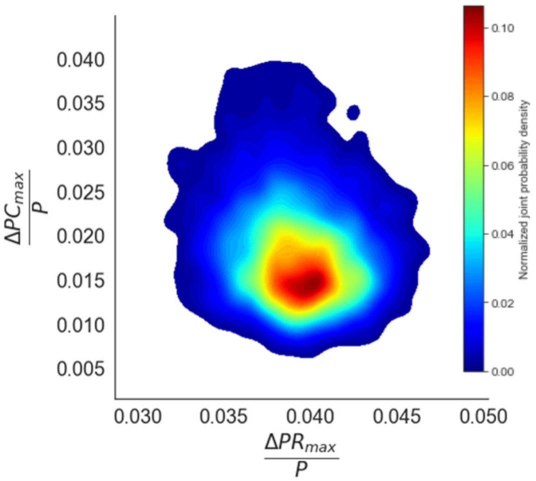

Fig. 8. Joint-PDF of value of circumferential pressure distortion and the value of the maximum radial pressure distortion.

For the radial pressure distortion, we will look at whether it is associated with a high circumferential pressure distortion value. Indeed, it is shown in Di-Marco et al. [52] that the radial pressure distortion is concentrated on the ring 5; therefore, looking at the distribution with regard to the ring will not give more information about the unsteadiness of the pressure field.

Fig. 8 shows the joint probability of the couple of parameters ΔPC_{max} and ΔPR_{max}. For this joint PDF, the resolution is about 0.0005 for ΔPC_{max} and 0.0005 for ΔPR_{max}. It can be seen that this radial pressure distortion is not associated with important circumferential pressure distortion values. Indeed, by looking at a circumferential distortion peak around 0.04, this value is associated with a radial distortion value around 0.04. On the other hand, the radial distortion peak is associated with values between 0.012

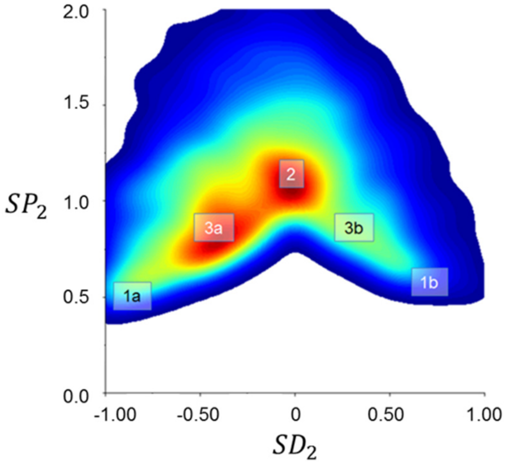

Fig. 9. Joint-PDF of the swirl directivity and pairs swirl descriptors on ring 2.

and 0.02. Therefore, peak values of circumferential pressure distortion are not synchronized with extreme radial distortion events.

The same type of analysis was performed by Gil-Prieto et al. [45] on an S-duct air intake, and similar conclusions were found concerning the link between circumferential pressure distortion and radial pressure distortion. However, the fluctuations of the radial position of the maximum circumferential pressure distortion were not reported in studies conducted on S-duct.

3.4. Unsteady swirl distortion characteristics

High level of swirl unsteadiness has been highlighted in the AIP plane in section 3.2. Therefore, a more detailed study on unsteady swirl distortion characteristics is proposed in this section. For this characterization, the swirl distortion is described using the swirl descriptors from the AIR5686 [5] and detailed in part 2.4 and in appendix B. From the Fig. 6a it can be seen that the most intense swirl area is located closest to the hub; therefore, to visualize the unsteadiness of the swirl in the AIP plane, all swirl parameters have been calculated on ring 2. The joint-PDF associated with the swirl pairs and the swirl directivity on ring 2 are shown in Fig. 9. The resolution is about 0.03 for SD2 and SP2.

Fig. 9 depicts two main zones with a high probability of having this pair of parameters. The first one is for the couple of parameters SP2=1 and SD2=0 (marked as zone 2 in Fig. 9). The second zone of high probability is the one marked as zone 3a in Fig. 9, this zone is characterized by a SP2=0.8 and a SD2=-0.4. To better understand the swirl pattern associated with these events, this joint-PDF has been separated into 5 distinct areas in order to look at the associated swirl pattern as well as the probability of occurrence. The two first zones, 1a and 1b, on Fig. 9 correspond to similar swirl patterns. Indeed, for zone 1a, the couple of parameters SD/SP are in the following range, SD2 goes through [-1;-0.75] and SP2 between [0.5;0.7]. According to the literature, the type of swirl associated with these two parameters is called a counter-clockwise bulk swirl or counter-swirl [5]. This means that on ring 2, there is one swirl zone rotating in the opposite direction compared to the compressor rotation. Fig. 10a shows the swirl pattern associated with these two parameters. It can be noticed that for the case studies, this couple of parameters corresponds to a vortical structure located at the upper side of the AIP plane. Fig. 10b corresponds to the swirl pattern associated with the couple SD2 going from [0.75;1] and a SP2 between [0.5;0.7] (zone 1b in Fig. 9). According to the literature, this type of swirl is called clockwise bulk swirl or co-swirl [5]. As for Fig. 10a this pattern is associated to one vortical structure but this one is located at the bottom side of the AIP plane and rotates in the opposite direction compared to the compressor. Zone 2, corresponding to an SD2 between [-0.25;0.25] and an SP2 between [0.9;1.1] is associated with a twin swirl pattern according to the AIR5686 report [5]. However, the associated pattern (Fig. 10c) shows two vortical structures, located on the upper and bottom sides of the AIP plane. Moreover, these two vortical structures have the particularity of having equal intensities. For zone 3a and 3b in Fig. 9, the same type of swirl pattern can be seen. The associated couple of parameters are SP2 between [0.75;0.9] with SD2 between [-0.5;-0.25] for zone 3a and SD2 between [0.25;0.5] for zone 3b. By looking at the pattern associated with these 2 zones, it can be seen that 2 vortical structures are identified, one at the top side of the AIP plane and the other at the bottom side. The difference between these two zones is the dominant vortical structure. Indeed, for zone 3a (Fig. 10d) the dominant vortical structure is located at the top side of the AIP plane, whereas it is located at the bottom side for zone 3b (Fig. 10e).

The probability of occurrence of each pattern could be calculated with equation (4) where X corresponds to SD2 and Y corresponds to SP2. The pattern 1a corresponding to Fig. 10a has a probability of occurrence of about 4% and 0.4% for the pattern associated with Fig. 10b. This means that this type of pattern can be qualified as a rare event. For the pattern corresponding to two vortical structures with one dominant over the other, the probability of occurrence of this type of pattern is about 20% for Fig. 10d and 10% for Fig. 10e. The probability of having two vortical structures with the same intensity (Fig. 10c) in the AIP plane is about 20%. This highlights an alternating vortex pattern between zones 2 and 3a because this calculation shows that there is almost the same probability of being in one of the zones. It can be noticed that the probability to have a complex swirl pattern with more than 2 vortical structures in the AIP plane is about 40%.

To conclude, the unsteady characteristics of swirl for an air intake with a plenum chamber can be compared to an S-duct air intake. Gil-Prieto et al. [28] highlighted a switching mode between a twin swirl pattern and a co-bulk swirl, or a counter bulk swirl. For air intake with a plenum chamber, this switching mode does not exist, and bulk swirl is qualified as a rare event. However, an alternating vortex pattern exists between the 2 vortical structures with equal intensity and 2 vortical structures with a dominant vortical structure located at the top side of the AIP plane. Moreover, it seems that the probability to have a more complex pattern is more important for an air intake with a plenum chamber.

3.5. Link between total pressure distortion and swirl

Swirl and pressure distortion are most of the time studied separately due to the high level of complexity required to experimentally control swirl distortion and total pressure distortion. However, recent studies show the importance of taking into account total pressure distortion and swirl distortion together [5]. Indeed, this study highlights the fact that pressure distortion coupled with counter-swirl interact in a non-linear way and drastically reduce the surge margin. Moreover, the type of swirl and also the position of the swirl distortion in the AIP plan have a different impact on compressor operability [63,14]. However, despite recent studies that have shown the necessity of treating swirl and pressure distortion together, only one study discusses the relationship between swirl and total pressure distortion. Gil-Prieto et al. [45] analyze the relationship between swirl and total pressure distortion using joint-PDF. The main objective of this study is to find a link between a peak event of swirl intensity and a peak event of circumferential or radial pressure distortion in an S-duct. Finally, this study concludes that peak events of swirl intensity and peak events of circumferential or radial pressure distortion are uncorrelated. To further investigate the relationship between swirl distortion and total pressure distortion, we have chosen to study the link between

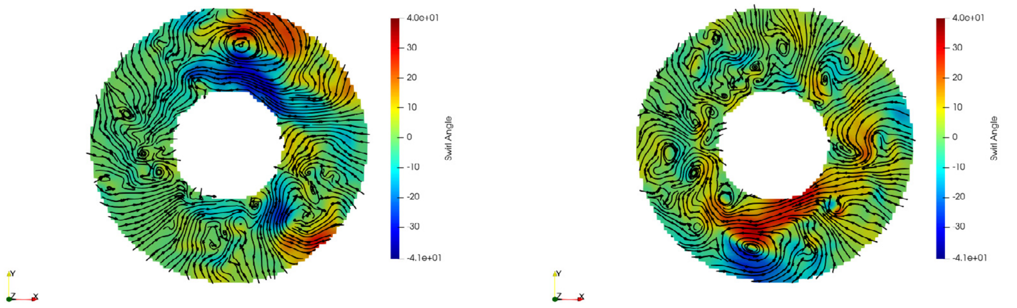

(a) Sector 1a (the probability of occurrence is about 4%, 120 events used for average)

(b) Sector 1b (the probability of occurrence is about 0.4%, 12 events used for average)

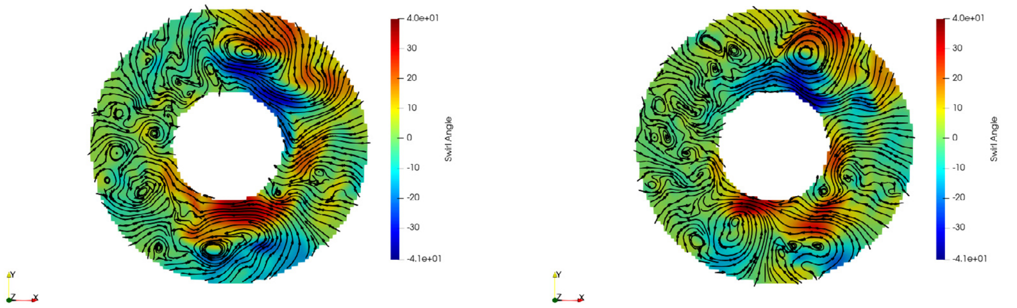

(c) Sector 2 (the probability of occurrence is about 20%, 600 events used for average)

(d) Sector 3a (the probability of occurrence is about 20%, 600 events used for average)

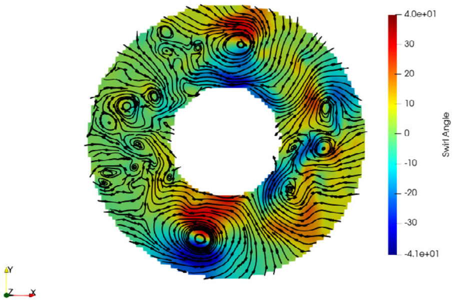

(e) Sector 3b (the probability of occurrence is about 10%, 300 events used for average)

Fig. 10. Swirl pattern associated to the different sector identified on Fig. 9.

the swirl pattern and the position of the maximum total pressure distortion in the AIP plane. The previous parts have shown a strong unsteadiness of the total pressure field as well as of the swirl angle in the AIP plane (Section 3.2). Section 3.3 has highlighted the fluctuation of the position of the maximum circumferential pressure distortion. Moreover, section 3.4 showed an alternating vortex pattern between a structure with two vortices of the same intensity and a structure with two vortices, one of which was dominant.

In this context, the purpose of the present section is to better understand the potential relationship between these two phenomena that were previously highlighted. First, a spectral analysis is performed, and then the swirl pattern associated with the position of the maximum circumferential pressure distortion is investigated.

Fig. 11 shows the power spectral density (PSD) of two different parameters. The first parameter SD2 allows to identify the characteristic frequency of the alternating vortex pattern highlighted previously since the previous part shows an alternance between a SD2 around 0 and a SD2 between -0.25 and -0.5. The second parameter, called ‘Ring, corresponds to the ring on which is located the maximum pressure distortion and allows to identify the

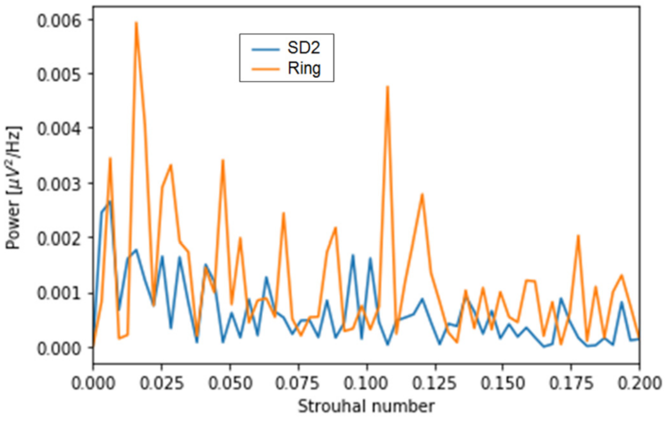

Fig. 11. Power spectral density of the overall time signal for swirl directivity on ring 2 (SD2) and the ring where the circumferential pressure distortion is maximum (where V correspond to the unit of SD2 and Ring).

characteristic frequency associated with the ring fluctuation highlighted in section 3.3. The power spectral density is computed using Welch [64] method and the sampling frequency is about 6000 Hz. It can be noticed that the alternating vortex pattern has a characteristic frequency of 4.3 Hz corresponding to St=0.01. For the fluctuation mode of the position of the maximum circumferential pressure distortion, the characteristic frequency is the same. However, even low frequency could affect surge margin, as highlighted in Freeman et al. [65]. Indeed, on Fig. 11 it can be seen that the two first peaks are located at the same frequency. However, the magnitude of the peak from PSD for 'Ring' is higher than the one for SD2. This spectral analysis highlights a potential link between the alternating vortex pattern and the position of the maximum circumferential pressure distortion.

Fig. 12 shows the joint-PDF of swirl descriptors (SD2 and SP2) when maximum circumferential pressure distortion is located on rings 3 and 5. It can be seen that when the maximum circumferential pressure distortion is located on ring 3 (see Fig. 12a), the couple SD2 and SP2 correspond to two vortical structures with equal intensity, one located on the top side and the other on the bottom side of the AIP plane (see Fig. 10c). On the other hand, Fig. 12b shows that the couple SD2 and SP2 correspond to a swirl distortion pattern highlight on Fig. 10d this means that there are two vortical structures located on the top and bottom sides of the AIP plane, with the one located on the top side being dominant over the other one.

To conclude this part, the relationship between the swirl distortion pattern and the position of the maximum circumferential pressure distortion in AIP has been highlighted. Indeed, the spectral analysis highlights the same characteristic frequency for the alternating vortex pattern highlighted in section 3.4 and the position of the maximum circumferential pressure distortion highlighted in section 3.3. Moreover, the joint-PDF applied to swirl descriptors allows associating a swirl pattern to a radial position of the maximum pressure distortion in the AIP plane. The swirl pattern associated with two vortical structures of equal intensity, one located on the top side and the other on the bottom, leads to a higher mean value of circumferential pressure distortion than the other swirl pattern and also to more severe peak distortion events.

4. Conclusion

The unsteady characteristics of flow distortion within a helicopter complex air intake, including a plenum chamber, have been investigated using a large eddy simulation lattice Boltzmann method. The simulation was performed on a complete geometry, including the helicopter geometry without a rotor equipped with an air intake on its right side. The flow structure inside the air intake was analyzed, and the mean flow distortion parameters in the AIP plane were validated with real flight test measurements. The unsteadiness of the flow distortion in the AIP plane was also analyzed through total pressure and swirl distortion coefficients. Complex distortion pattern associated to important unsteadiness effect were highlighted for both total pressure and swirl. Therefore, the unsteady characteristics of pressure and swirl distortion were assessed using conventional descriptors, namely $\frac{\Delta PC}{P}$, $\frac{\Delta PR}{P}$ for pressure distortion and SI, SP, SD for swirl distortion.

The pressure distortion analysis permitted highlighting a fluctuation between two positions of the maximum circumferential pressure distortion between rings 3 and 5 using joint-PDF. However, the probability that the maximum circumferential pressure is located in ring 3 is higher than in ring 5. Moreover, the pressure distortion level associated with the position of the maximum circumferential pressure distortion shows that on ring 3, the pressure distortion level is greater than on ring 5, and the peak of distortion is also higher. Indeed, there is 68.2% of probability that a circumferential pressure distortion level will be higher on ring 3 than on ring 5. The maximum peak of circumferential pressure distortion identified on ring 3 is 3.5 times higher than the one reached on ring 5. It should be noted that the peak value of circumferential pressure distortion is not synchronized with the peak value of radial distortion. The swirl distortion analysis permitted to highlight the presence of two vortical structures located on the top and bottom sides of the AIP plane. An alternating vortex pattern has also been identified between two swirl distortion patterns. The first mode found is a mode where the two vortical structures are of equal intensity. The other mode identified is a mode where the vortex structure located in the top side of AIP plane dominate the other vortex structure. Moreover, these two modes have the same probability of appearing.

Finally, the relationship between pressure distortion and swirl distortion is investigated. The bibliographic review highlights the necessity of taking into account pressure distortion and swirl distortion together to assess the loss of surge margin. However, experimental studies are complex, and CFD analysis seems to be the best alternative for the study of these phenomena together. Therefore, the relationship between the position of the circumferential distortion, which is linked to the maximum value reached for this parameter, and the swirl distortion pattern is assessed using a spectral analysis. The spectral analysis highlights the same characteristic frequency for the fluctuation previously identified for pressure and swirl distortion. Then joint-PDF applied to each ring confirms the link found by spectral analysis. Indeed, a swirl pattern associated to a ring position is highlighted, the swirl pattern corresponding to a two vortical structure with equal intensity leads to a maximum circumferential pressure distortion. On the other hand, a two vortical structure with top side structure dominating leads to a position of circumferential pressure distortion on ring 5.

Consequently, the demonstration of the relationship between pressure and swirl distortion allows geometrical changes of the air intake in order to have a higher probability of occurrence of a swirl pattern corresponding to two vortical structures with the one located on the top side of the AIP plane dominant. This geometrical change will allow a reduction of the circumferential pressure distortion but also a reduction of the maximum peak reachable during this phase of flight. To go further, a parametric study especially on the plenum chamber could be performed to determine geometric parameters that have an impact on the swirl distortion pattern but also on dynamics distortion. Moreover, LBM could be used to assess the sensitivity of unsteady flow distortion characteristics with flight conditions such as aircraft position (pitch, roll, yaw) that would impact the structure and turbulent content of the flow ingested by the air intake.

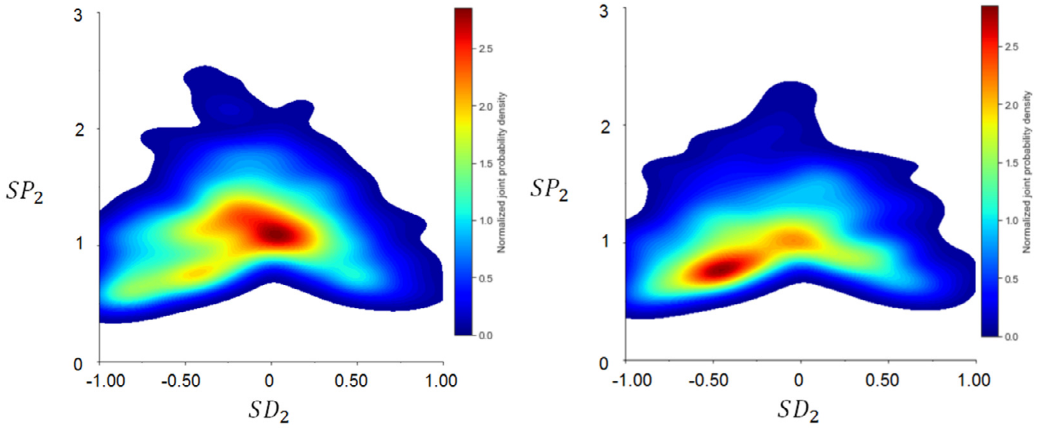

(a) Circumferential pressure distortion located on ring 3

(b) Circumferential pressure distortion located on ring 5

Fig. 12. Joint-PDF of swirl descriptors applied to a maximum circumferential pressure distortion located on ring 3 and ring 5.

To conclude, this work shows the advantages of the LBM method, which allows unsteady calculations on complex geometries in an industrial context, as well as the usefulness of doing unsteady calculations on the air intake. Moreover, this analysis can be performed early in the design phase and can help to improve the design of the air intake as well as make the air intake more robust to the unsteadiness of the flow field.

Declaration of competing interest

The authors declare the following financial interests/personal relationships which may be considered as potential competing interests: DI-MARCO Alexandre reports financial support was provided by Airbus Helicopters. DI-MARCO Alexandre reports a relationship with Airbus Helicopters that includes: employment.

Data availability

The data that has been used is confidential.

Acknowledgements

The authors want to thank Airbus Helicopters for providing geometry and HPC resources. The author also wants to thank CS for providing LBpre software for pre-processing computation.

Appendix A. Pressure distortion descriptors

In part 2.4 several parameters are proposed. However, in this paper, only three parameters are used to describe pressure distortion. The first one is based on the Rolls Royce critical angle DC_θ with a critical angle of 60 degrees as proposed by [66].

$$DC_{60} = \frac{P_{t60^\circ,min} - P_{t,mean}}{\frac{1}{2}\rho V^2} \tag{A.1}$$

However, in this paper, DC_{60} is only used to validate the CFD computation against the flight test. Indeed, this parameter is not sufficient to describe the pressure field in the AIP plane since different pressure fields can lead to the same DC_{60} value. Therefore, other parameters have been developed [2] to describe the pressure distribution in the AIP plane, ring by ring, which allow to quantify separately circumferential and radial distortion. The circumferential distortion is described by three parameters, the intensity ($\frac{\Delta PC}{P}$), extent (θ^-), and multiple-per-revolution (MPR) values.

The extent is defined as the circumferential extent of the low pressure region for the i^{th} ring. Usually, the extent is expressed in degrees. This parameter provides information on how long the compressor blade remains in the low pressure zone for one revolution.

$$(\theta^-)_i = \theta_{2_i} - \theta_{1_i} \tag{A.2}$$

Sometimes several low pressure areas appear on a ring. In this case θ_i^- is defined by the equation,

$$(\theta_k^-)_i = \sum_{k=1}^{LP} (\theta_k^-)_i \tag{A.3}$$

where Lp corresponds to the number of low pressure areas in a ring. When low pressure areas are separated by high pressure areas (θ^+) lower than θ^+_{min} then the low pressure area is considered as a single low pressure area. AIR1419 [2] recommends $\theta^+_{min} <= 25°$.

The amplitude of the circumferential distortion is also an important parameter and is defined for each ring i as

$$\left(\frac{\Delta PC}{P}\right)_i = \left(\frac{(P_t)_i - (P_{t,low})_i}{(P_t)_i}\right) \tag{A.4}$$

with

$$(Pt_{,low})_i = \frac{1}{\theta_i^-} \int_{\theta_i^-} P_t(\theta)_i \mathrm{d}\theta \tag{A.5}$$

and Pt_i the average pressure on the i^{th} ring. As for the extent, when several low pressure areas are present in a ring, the intensity of the distortion is defined by this equation.

$$\left(\frac{\Delta PC}{P}\right)_{k,i} = \frac{\sum_{k=1}^{LP} \left(\frac{\Delta PC}{P}\right)_{k,i} (\theta_k^-)_i}{\sum_{k=1}^{LP} (\theta_k^-)_i} \tag{A.6}$$

To conclude with circumferential distortion, the multiple-per-revolution (MPR) parameter is used to describe the number of low pressure areas in a ring.

$$MPR_i = \frac{\sum_{k=1}^{LP} \left(\frac{\Delta PC}{P}\right)_{k,i} (\theta_k^-)_i}{max\left[\left(\frac{\Delta PC}{P}\right)_{k,i} (\theta_k^-)_i\right]} \tag{A.7}$$

As well as circumferential distortion, radial distortion can be calculated for each ring using equation (A.8)

In this paper, radial distortions at the hub and tip are defined as follows:

$$\left(\frac{\Delta PR}{P}\right)_{hub} = \left(\frac{\Delta PR}{P}\right)_1 \quad \text{and} \quad \left(\frac{\Delta PR}{P}\right)_{tip} = \left(\frac{\Delta PR}{P}\right)_5 \tag{A.8}$$

According to the equation (A.8) the radial distortion at the hub will be negative while the radial distortion at the tip will be positive.

Appendix B. Swirl distortion descriptors

As well as pressure and temperature distortion, swirl distortion has an impact on the performance and stability margin of the engine. The Society of Automotive Engineers proposed through the AIR 5686 [5] report several parameters that allow to define the swirl distortion in the AIP plane. All these descriptors are based on the swirl angle distribution on each ring. The swirl angle is defined by the following equation:

$$\alpha = tan^{-1}\left(\frac{U_\theta}{U_x}\right) \tag{B.1}$$

A positive swirl angle corresponds to a tangential speed that goes in the same direction as the rotation of the compressor, while a negative swirl angle corresponds to a tangential speed that goes in the opposite direction of the rotation of the compressor. Therefore, swirl sector elements are defined by SS_i^+ for positive swirl and SS_i^- for negative swirl.

$$SS_i^+ = \frac{1}{\theta_i^+}\int\limits_{\theta_i^+} \alpha(\theta)_i \mathrm{d}\theta \tag{B.2}$$

$$SS_i^- = \frac{1}{\theta_i^-}\int\limits_{\theta_i^-} \alpha(\theta)_i \mathrm{d}\theta \tag{B.3}$$

The swirl amplitude is defined using the SI parameter, which corresponds to the absolute intensity of the swirl on a ring. In the case of multiple-per-rev, swirl distortion is estimated as follows:

$$SI_i = \frac{\sum_{k=1}^{s} SS_i^+\theta_i^+ + \sum_{k=1}^{s} |SS_i^-|\theta_i^-}{360} \tag{B.4}$$

where s is the number of swirl sectors on the i^{th} ring. Another important parameter is the Swirl Directivity (SD) which corresponds to the swirl rotational direction. In the case of multiple-per-rev swirl distortion, swirl directivity is defined as follows:

$$SD_i = \frac{\sum_{k=1}^{s} SS_i^+\theta_i^+ + \sum_{k=1}^{s} SS_i^-\theta_i^-}{\sum_{k=1}^{s} SS_i^+\theta_i^+ + \sum_{k=1}^{s} |SS_i^-|\theta_i^-} \tag{B.5}$$

A pure bulk swirl will be described by a swirl directivity equal to 1 for a co-swirl and -1 for a counter swirl. For paired swirl SD equal to 0, mean that all positive swirl amplitudes are the same as the amplitudes of all negative swirl present in the i^{th} ring.

The swirl pairs parameter (SP) gives information about the number of pairs of alternating swirls present in a ring.

$$SP_i = \frac{\sum_{k=1}^{s} SS_i^+\theta_i^+ + \sum_{k=1}^{s} |SS_i^-|\theta_i^-}{2 \times Max\left[SS_i^+\theta_i^+, |SS_i^-|\theta_i^-\right]_{k=1\ to\ s}} \tag{B.6}$$

These values can vary from 0.5 for a pure swirl pattern in a ring to 2 or more for multiple-per-rev patterns.

References

[1] Society of Automotive Engineers, S-12 Powered Lift Propulsion Committee, the effect of installation power losses on the overall performance of a helicopter, Technical Report AIR 5642, 2005.

[2] Society of Automotive Engineers, Inlet total-pressure-distortion considerations for gas-turbine engines, https://doi.org/10.4271/AIR1419C, Nov 2017.

[3] E.J. Gunn, S.E. Tooze, C.A. Hall, Y. Colin, An experimental study of loss sources in a fan operating with continuous inlet stagnation pressure distortion, J. Turbomach. 135 (5) (2013) 051002, https://doi.org/10.1115/1.4007835.

[4] Society of Automotive Engineers, Assessment of the inlet/engine total temperature distortion problem, https://doi.org/10.4271/AIR5867, Nov 2017.

[5] Society of Automotive Engineers, A methodology for assessing inlet swirl distortion, https://doi.org/10.4271/AIR5686, Mar 2022.

[6] Society of Automotive Engineers, Gas turbine engine inlet flow distortion guidelines, https://doi.org/10.4271/ARP1420C, Apr 2017.

[7] W.T. Cousins, History, Philosophy, Physics, and Future Directions of Aircraft Propulsion System/Inlet Integration, Turbo Expo: Power for Land, Sea, and Air, vol. 41677, 2004, pp. 305–320.

[8] W. Braithwaite, E. Graber Jr., C. Mehalic, The effect of inlet temperature and pressure distortion on turbojet performance, in: 9th Propulsion Conference, 1973, p. 1316.

[9] R.H. Soeder, G.A. Bobula, Effect of steady-state pressure distortion on flow characteristics entering a turbofan engine, in: NASA TM-79134, 1979.

[10] F. Aulehla, Intake swirl- a major disturbance parameter in engine/intake compatibility, in: AIAA, 1290 Ave. Americas, New York, NY 10104, USA, 1982, 1982.

[11] Society of Automotive Engineers, An assessment of planar waves, https://doi.org/10.4271/AIR5866A, Feb 2021.

[12] Y. Sheoran, B. Bouldin, R. Hoover, M. Matwey, A Centrifugal Compressor Operability Correlation with Combined Total Pressure and Swirl Distortion, Turbo Expo: Power for Land, Sea, and Air, vol. 50770, American Society of Mechanical Engineers, 2017, p. V001T01A015.

[13] B. Tu, L. Zhang, J. Hu, Effect of swirl on the performance and stability of transonic axial compressor, Proc. Inst. Mech. Eng. A, J. Power Energy 232 (6) (2018) 608–621, https://doi.org/10.1177/0957650917742320.

[14] N. Fredrick, M. Davis, Investigation of the effects of inlet swirl on compressor performance and operability using a modified parallel compressor model, in: ASME 2011 Turbo Expo: Turbine Technical Conference and Exposition, American Society of Mechanical Engineers Digital Collection, 2011, pp. 177–187.

[15] M. Davis, A. Hale, D. Beale, An argument for enhancement of the current inlet distortion ground test practice for aircraft gas turbine engines[1], J. Turbomach. 124 (2) (2002) 235–241, https://doi.org/10.1115/1.1451087, https://asmedigitalcollection.asme.org/turbomachinery/article-pdf/124/2/235/6838306/235_1.pdf.

[16] J.P. Longley, H.W. Shin, R.E. Plumley, P.D. Silkowski, I.J. Day, E.M. Greitzer, C.S. Tan, D.C. Wisler, Effects of rotating inlet distortion on multistage compressor stability, J. Turbomach. 118 (2) (1996) 181–188, https://doi.org/10.1115/1.2836624, https://asmedigitalcollection.asme.org/turbomachinery/article-pdf/118/2/181/5501129/181_1.pdf.

[17] C. Tan, I. Day, S. Morris, A. Wadia, Spike-type compressor stall inception, detection, and control, Annu. Rev. Fluid Mech. 42 (1) (2010) 275–300, https://doi.org/10.1146/annurev-fluid-121108-145603.

[18] L. Adrian, R.J. Adrian, J. Westerweel, Particle Image Velocimetry, vol. 30, Cambridge University Press, 2011.

[19] U. Doll, M. Migliorini, J. Baikie, P.K. Zachos, I. Röhle, S. Melnikov, J. Steinbock, M. Dues, R. Kapulla, D.G. MacManus, et al., Non-intrusive flow diagnostics for unsteady inlet flow distortion measurements in novel aircraft architectures, Prog. Aerosp. Sci. 130 (2022) 100810, https://doi.org/10.1016/j.paerosci.2022.100810.

[20] J. Jacocks, Statistical analysis of distortion factors, in: 8th Joint Propulsion Specialist Conference, 1972, p. 1100.

[21] F. Aulehla, D. Schmitz, New trends in intake/engine compatibility assessment, Tech. Rep., Messerschmitt-Boelkow-Blohm Gmbh Munich (Germany Fr) Helicopter and Military ..., 1987.

[22] R. Borg, A synthesis method for estimating maximum instantaneous inlet distortion based on measured inlet steady state and RMS pressures, in: AGARD Aerodyn. of Power Plant Installation, 1981, 12 p. (see N 82-13065 04-01).

[23] D. Liang, S. Zhang, Improved method for estimation of the maximum instantaneous distortion values, J. Propuls. Power 10 (4) (1994) 522–526, https://doi.org/10.2514/3.23803.

[24] G. Tanguy, D.G. MacManus, E. Garnier, P.G. Martin, Characteristics of unsteady total pressure distortion for a complex aero-engine intake duct, Aerosp. Sci. Technol. 78 (2018) 297–311.

[25] M.T. Lakebrink, M. Mani, Numerical investigation of dynamic distortion and flow control in a serpentine diffuser, in: 2018 AIAA Aerospace Sciences Meeting, 2018, p. 1283.

[26] F.-Q. Chen, X.-S. Li, B. Hu, X.-D. Ren, Z.-Y. Wang, C.-W. Gu, Pressure drop analysis and aerodynamic design of compressor L-inlet duct, Aerosp. Sci. Technol. 107 (2020) 106324, https://doi.org/10.1016/j.ast.2020.106324.

[27] S.R. Wellborn, B.A. Reichert, T.H. Okiishi, Study of the compressible flow in a diffusing S-duct, J. Propuls. Power 10 (5) (1994) 668–675, https://doi.org/10.2514/3.23778.

[28] D. Gil-Prieto, D.G. MacManus, P.K. Zachos, G. Tanguy, K.R. Menzies, Convoluted intake distortion measurements using stereo particle image velocimetry, AIAA J. 55 (6) (2017) 1878–1892, https://doi.org/10.2514/1.J055467.

[29] M. Migliorini, P.K. Zachos, D.G. MacManus, V. Monnier, A study on the development of the flow distortion downstream of an S-duct intake, in: 33rd Congress of the International Council of the Aeronautical Sciences, ICAS, 2022, https://dspace.lib.cranfield.ac.uk/handle/1826/18447.

[30] M. Migliorini, P.K. Zachos, D.G. MacManus, P. Haladuda, S-duct flow distortion with non-uniform inlet conditions, Proc. Inst. Mech. Eng., G J. Aerosp. Eng. (2022) 09544100221101669, https://doi.org/10.1177/09544100221101669.

[31] X. Han, T.J. Wray, C. Fiola, R.K. Agarwal, Computation of flow in s ducts with Wray–Agarwal one-equation turbulence model, J. Propuls. Power 31 (5) (2015) 1338–1349.

[32] C. Fiola, R.K. Agarwal, Simulation of secondary and separated flow in a diffusing s-duct using four different turbulence models, Proc. Inst. Mech. Eng., G J. Aerosp. Eng. 228 (11) (2014) 1954–1963, https://doi.org/10.1177/0954410013507249.

[33] C. Fiola, R.K. Agarwal, Simulation of secondary and separated flow in diffusing s ducts, J. Propuls. Power 31 (1) (2015) 180–191.

[34] P. Aref, M. Ghoreyshi, A. Jirasek, M.J. Satchell, CFD validation and flow control of RAE-M2129 S-duct diffuser using CREATETM-AV kestrel simulation tools, Aerospace 5 (1) (2018) 31, https://doi.org/10.3390/aerospace5010031.

[35] A.-L. Delot, R. Scharnhorst, A comparison of several CFD codes with experimental data in a diffusing S-duct, in: 49th AIAA/ASME/SAE/ASEE Joint Propulsion Conference, 2013, https://arc.aiaa.org/doi/abs/10.2514/6.2013-3796.

[36] W. Zhang, M. Vahdati, A parametric study of the effects of inlet distortion on fan aerodynamic stability, J. Turbomach. 141 (1) (2019) 011011, https://doi.org/10.1115/1.4041376.

[37] T. Piovesan, W. Zhang, M. Vahdati, P. Zachos, Investigations of the unsteady aerodynamic characteristics for intakes at crosswind, in: Proceedings of the ASME Turbo Expo 2022: Turbomachinery Technical Conference and Exposition, vol. 10C, ASME, 2022, p. V10CT33A009.

[38] L.S. Lima, R. Huebner, L. Tobaldini, Numerical investigations of s-shaped air inlet for embedded engines, J. Propuls. Power 35 (2) (2019) 475–489, https://doi.org/10.2514/1.B36949.

[39] A. Batista de Jesus, L. Trapp, D. Abreu, A. Lombardi, L. Tobaldini, Grid topology study of the s-duct inlet with vortex generators, in: 51st AIAA/SAE/ASEE Joint Propulsion Conference, 2015, p. 3962.

[40] A. Garbo, B. German, Comparison of adaptive design space exploration methods applied to s-duct cfd simulation, in: 57th AIAA/ASCE/AHS/ASC Structures, Structural Dynamics, and Materials Conference, 2016, p. 0416.

[41] M.M. Wojewodka, C. White, S. Shahpar, K. Kontis, A review of flow control techniques and optimisation in s-shaped ducts, Int. J. Heat Fluid Flow 74 (2018) 223–235, https://doi.org/10.1016/j.ijheatfluidflow.2018.07.006.

[42] G. Tanguy, D.G. MacManus, E. Garnier, Numerical investigation of the unsteady distortion for an S-duct intake with mechanical vortex generators, Int. J. Heat Fluid Flow 95 (2022) 108975, https://doi.org/10.1016/j.ijheatfluidflow.2022.108975.

[43] M.M. Wojewodka, C. White, S. Shahpar, K. Kontis, Numerical study of complex flow physics and coherent structures of the flow through a convoluted duct, Aerosp. Sci. Technol. 121 (2022) 107191, https://doi.org/10.1016/j.ast.2021.107191.

[44] D.G. MacManus, N. Chiereghin, D.G. Prieto, P. Zachos, Complex aeroengine intake ducts and dynamic distortion, AIAA J. 55 (7) (2017) 2395–2409, https://doi.org/10.2514/1.J054905.

[45] D. Gil-Prieto, D.G. MacManus, P.K. Zachos, A. Bautista, Assessment methods for unsteady flow distortion in aero-engine intakes, Aerosp. Sci. Technol. 72 (2018) 292–304, https://doi.org/10.1016/j.ast.2017.10.029.

[46] S. Wilhelm, J. Jacob, P. Sagaut, A new explicit algebraic wall model for LES of turbulent flows under adverse pressure gradient, Flow Turbul. Combust. 106 (1) (2021) 1–35, https://doi.org/10.1007/s10494-020-00181-7.

[47] Y. Hou, D. Angland, A. Sengissen, A. Scotto, Lattice-Boltzmann and Navier-Stokes simulations of the partially dressed, cavity-closed nose landing gear benchmark case, in: 25th AIAA/CEAS Aeroacoustics Conference, 2019, p. 2555.

[48] J.-M. Lucas, O. Cadot, V. Herbert, S. Parpais, J. Délery, A numerical investigation of the asymmetric wake mode of a squareback Ahmed body–effect of a base cavity, J. Fluid Mech. 831 (2017) 675–697, https://doi.org/10.1017/jfm.2017.654.

[49] M. Guerrero-Hurtado, P. Zachos, D. MacManus, M. Migliorini, G. Trapani, Unsteady swirl distortion characteristics for S-ducts using lattice Boltzmann and time-resolved, stereo PIV methods, in: AIAA Propulsion and Energy 2019 Forum, 2019, p. 4275.

[50] F. Knoth, C. Breitsamter, Flow analysis of a helicopter engine side air intake, J. Propuls. Power 33 (5) (2017) 1230–1244, https://doi.org/10.2514/1.B36285.

[51] A. Di-Marco, C. Lecauchois, B. Fayard, P. Sagaut, A predictive method for helicopters engine installation losses determination, in: Proceedings of the ASME Turbo Expo 2022: Turbomachinery Technical Conference and Exposition. Volume 1: Aircraft Engine; Ceramics and Ceramic Composites, Turbo Expo: Power for Land, Sea, and Air, 2022.

[52] A. Di-Marco, C. Lecauchois, B. Fayard, P. Sagaut, Helicopters engine integration: from CFD deep airflow analysis to general impact on helicopter engine performance, in: AIAA AVIATION 2022 Forum, 2022.

[53] N. Afzal, Wake layer in a turbulent boundary layer with pressure gradient: a new approach, in: IUTAM Symposium on Asymptotic Methods for Turbulent Shear Flows at High Reynolds Numbers, Kluwer Academic Publishers, Bochum, Germany, 1996, pp. 95–118.

[54] T. Krüger, H. Kusumaatmaja, A. Kuzmin, O. Shardt, G. Silva, E. Viggen, The Lattice Boltzmann Method. Principles and Practice, Springer, 2017.

[55] J. Jacob, O. Malaspinas, P. Sagaut, A new hybrid recursive regularised Bhatnagar–Gross–Krook collision model for lattice Boltzmann method-based large eddy simulation, J. Turbul. 19 (11–12) (2018) 1051–1076, https://doi.org/10.1080/14685248.2018.1540879.

[56] E. Lévêque, F. Toschi, L. Shao, J.-P. Bertoglio, Shear-improved Smagorinsky model for large-eddy simulation of wall-bounded turbulent flows, J. Fluid Mech. 570 (2007) 491–502, https://doi.org/10.1017/S0022112006003429.

[57] S. Wilhelm, J. Jacob, P. Sagaut, An explicit power-law-based wall model for lattice Boltzmann method–Reynolds-averaged numerical simulations of the flow around airfoils, Phys. Fluids 30 (6) (2018) 065111, https://doi.org/10.1063/1.5031764.

[58] A.P. Farr, Evaluation of F-15 inlet dynamic distortion, J. Aircr. 13 (1) (1976) 36–42.

[59] J. Boytos, State-of-the-art review: Aircraft gas turbines–inlet distortion indices, Tech. Rep., NAPTC-PE-95, March 1977.

[60] R. Hercock, D. Williams, Aerodynamic response, in: AGARD Distortion Induced Eng. Instability, 1974, 41 p. (see N 75-12954 04-07).

[61] M.T. Moore, Distortion data analysis, Tech. Rep., General Electric Co Cincinnati Oh Aircraft Engine Business Group, 1973.

[62] J. Li, J. Du, Y. Liu, H. Zhang, C. Nie, Effect of inlet radial distortion on aerodynamic stability in a multi-stage axial flow compressor, Aerosp. Sci. Technol. 105 (2020) 105886, https://doi.org/10.1016/j.ast.2020.105886.

[63] A. Mehdi, Effect of swirl distortion on gas turbine operability, Ph.D. thesis, Cranfield University, 2014.

[64] P. Welch, The use of fast Fourier transform for the estimation of power spectra: a method based on time averaging over short, modified periodograms, IEEE Trans. Audio Electroacoust. 15 (2) (1967) 70–73, https://doi.org/10.1109/TAU.1967.1161901.

[65] C. Freeman, A.L. Rowe, Intake Engine Interactions of a Modern Large Turbofan Engine, Turbo Expo: Power for Land, Sea, and Air, vol. 78583, American Society of Mechanical Engineers, 1999, p. V001T01A007.

[66] J. Kurzke, I. Halliwell, Inlet Flow Distortion, Springer International Publishing, 2018, pp. 249–267.